CHEMISTRY

Atomically deviated Pd-Te nanoplates boost methanol-tolerant fuel cells

Ying Zhang[1]*, Bolong Huang[2]*, Gan Luo[3]*, Tu Sun[4]*, Yonggang Feng[1], Yucheng Wang[5], Yanhang Ma[4†], Qi Shao[1], Yafei Li[3†], Zhiyou Zhou[5], Xiaoqing Huang[1†]

The methanol crossover effect in direct methanol fuel cells (DMFCs) can severely reduce cathodic oxygen reduction reaction (ORR) performance and fuel efficiency. As a result, developing efficient catalysts with simultaneously high ORR activity and excellent antipoisoning methanol capability remains challenging. Here, we report a class of Pd-Te hexagonal nanoplates (HPs) with a $Pd_{20}Te_7$ phase that simultaneously overcome the activity and methanol-tolerant issues in alkaline DMFC. Because of the specific arrangement of Pd atoms deviated from typical hexagonal close-packing, Pd-Te HPs/C displays extraordinary methanol tolerance with high ORR performance compared with commercial Pt/C. DFT calculations reveal that the high performance of Pd-Te HPs can be attributed to the breakthrough of the linear relationship between OOH* and OH* adsorption, which leaves sufficient room to improve the ORR activity but suppresses the methanol oxidation reaction. The concurrent high ORR activity and excellent methanol tolerance endow Pd-Te HPs as practical electrocatalysts for DMFC and beyond.

INTRODUCTION

Direct methanol fuel cells (DMFCs), as clean energy-converting devices for various applications, have drawn extensive research attention in recent years because of their high efficiency, high energy density, and extremely low emissions (1–10). Despite these advantages, however, one critical issue in DMFCs, namely, the methanol crossover effect, must be overcome before commercialization. Noble metals (e.g., Pt and Pd) are still regarded as the best cathodic oxygen reduction reaction (ORR) catalysts, but it is difficult to simultaneously achieve desirable methanol tolerance and high ORR activity for most reported Pt/Pd-based nanomaterials (11–16). The methanol permeation from the anode to cathode will be oxidized and cause mixed potential at the cathode, which consequently induces severe noble metal poisoning because of the strong adsorption of the CO-like species (by-products of methanol oxidation) on the noble metal surface (17, 18). This phenomenon critically reduces the cathodic ORR performance and lowers fuel efficiency. Therefore, developing cathode catalysts with simultaneous superior ORR activity and excellent methanol tolerance is highly desirable yet extremely challenging.

In principle, the idea behind addressing this challenge is to achieve appropriate chemisorption of O_2 while eliminating chemisorption of the poisoning species on the catalyst surface. To this end, Pt-based catalysts with intermetallic structures have attracted intensive research interests that have exhibited improved methanol tolerance via notably reducing bridge sites and elim-

inating threefold hollow adsorption sites of Pt (19, 20). However, the enhanced antipoisoning properties of those catalysts are realized by sacrificing activity because O_2 chemisorption and O–O bond breakage, vital processes for efficient ORR, require two adjacent atom sites (21). Therefore, to construct a unique structure to effectively achieve the selective chemisorption between O_2 and the poisoning species is highly desirable but challenging. There is still much room to improve ORR catalysis with enhanced methanol tolerance.

In recent years, Pt group metal chalcogenides have attracted considerable attention because of their relevance in catalysis and materials science (22–24). Binary Pd and Pt chalcogenides show a higher diversity of structures and unique physical and chemical properties. Pt dichalcogenides are inherent layered compounds with two-dimensional (2D) PtX_2 (X = S, Se, and Te) monolayers that are weakly stacked by van der Waals' interactions. With these unique structures, Pt dichalcogenides have promising properties for several applications. For example, Pt dichalcogenides have been reported to display competent electrocatalytic performance for the hydrogen evolution reaction in comparison with Pt/C (25), while the Pt-Te monolayer shows excellent catalytic activity toward ORR as predicted by simulations (26). Here, we report that Pd-Te hexagonal nanoplates (HPs) can be adopted as highly efficient electrocatalysts for ORR with a robust antipoisoning methanol feature. As a starting point, the well-defined Pd-Te HPs with a $Pd_{20}Te_7$ phase have been successfully prepared. The Pd atoms in the Pd-Te nanoplates are in a deviated hexagonal close-packed arrangement, which provides bridge sites for active catalysis centers but no effective hollow sites. Consequently, the unique Pd-Te HPs/C shows promising ORR activity and long-time durability with negligible activity decay and limited structure changes. Notably, Pd-Te HPs/C displays extraordinary methanol tolerance with high ORR activity in alkaline DMFC, outperforming those of commercial Pt/C. X-ray photoelectron spectroscopy (XPS) results further show that the strong electronic interactions between Pd and Te in Pd-Te HPs result in more available Pd sites for enhanced ORR. In addition, diffuse reflectance infrared Fourier transform spectroscopy (DRIFTS) indicates that the Pd-Te HPs/C is very inert to CH_3OH dissociation activation. The simulations further revealed that the

[1]College of Chemistry, Chemical Engineering and Materials Science, Soochow University, Jiangsu 215123, China. [2]Department of Applied Biology and Chemical Technology, The Hong Kong Polytechnic University, Hung Hom, Kowloon, Hong Kong SAR. [3]Jiangsu Collaborative Innovation Centre of Biomedical Functional Materials, Jiangsu Key Laboratory of New Power Batteries, School of Chemistry and Materials Science, Nanjing Normal University, Nanjing 210023, China. [4]School of Physical Science and Technology, Shanghai Tech University, Shanghai 201210, China. [5]State Key Laboratory of Physical Chemistry of Solid Surfaces, Collaborative Innovation Center of Chemistry for Energy Materials, College of Chemistry and Chemical Engineering, Xiamen University, Xiamen 361005, China.
*These authors contributed equally to this work.
†Corresponding author. Email: mayh2@shanghaitech.edu.cn (Y.M.); liyafei@njnu.edu.cn (Y.L.); hxq006@suda.edu.cn (X.H.)

superior ORR activity of Pd-Te should be intrinsically attributed to the breakthrough of the linear relation between OOH* and OH* adsorption, while the methanol oxidation reaction (MOR) process on Pd-Te is highly endothermic.

RESULTS AND DISCUSSION

The synthesis of Pd-Te HPs was achieved in aqueous conditions by using palladium (II) acetylacetonate [Pd(acac)$_2$] and telluric (VI) acid (H$_6$TeO$_6$) as the metal precursors, N,N-dimethylacetamide (DMAC) as solvent, polyvinylpyrrolidone (PVP) as surfactant, and in the presence of citric acid (CA) and ammonium chloride (NH$_4$Cl) (details in the Supplementary Materials). Their morphology was initially characterized by high-angle annular dark-field scanning transmission electron microscopy (HAADF-STEM). As shown in Fig. 1 (A and B), the HPs are the dominant products with a yield approaching 90%. The HPs are highly dispersive, with the edge length of approximately 50 nm (fig. S1). The atomic ratio of Pd to Te is ~2.6: 1, as confirmed by scanning electron microscopy energy-dispersive x-ray spectroscopy (SEM-EDS) (fig. S2), close to the feeding amounts of Pd(acac)$_2$ and H$_6$TeO$_6$. Next, a series of time-tracking experiments were carried out to study the reaction kinetics by analyzing the concentrations of Pd and Te remaining in the reaction solution at different reaction time, which shows that the atomic ratio of Pd and Te is very close to the feeding ratio, indicating that the reduction kinetics of Pd and Te in the present synthesis process is similar (fig. S3). The elemental distributions of Pd and Te in HPs were characterized by EDS mapping (Fig. 1C), where the Pd (red), Te (green), and overlap (red versus green) images collectively show that Pd and Te are highly even throughout the HPs, which is consistent with the line-scan analysis results (Fig. 1D). To further analyze the distributions of Pd and Te, we measured the EDS mapping by rotating the angle of positive 30° and negative 30°, respectively. It

can be seen that the distributions of Pd and Te along different angles are all uniform (fig. S4). Figure 1E shows an atomic force microscopy (AFM) image of Pd-Te HPs, where the section analysis and height profile (Fig. 1, F to G) reveal that the thickness of Pd-Te HPs is approximately 19 nm. The above results collectively confirm that Pd-Te HPs have characteristics of uniform distributions of Pd and Te and a hexagonal shape with even thicknesses.

As shown in Fig. 2A, the typical selected area electron diffraction (SAED) pattern viewed perpendicular to the plate shows a sixfold rotation symmetry and the lattice constant 6.0 Å of the closest diffraction spot. As the phase cannot be identified directly using either powder x-ray diffraction (PXRD) or SAED data, 3D electron diffraction tomography (3D-EDT) was used to obtain an ab initio structure solution (27). One EDT data set was collected from a single Pd-Te by combining specimen tilt and electron beam tilt in the range of −60.5° to +58.7° with a beam-tilt step of 0.2°. The positions and intensities of observed reflections were reconstructed in 3D reciprocal space using 688 electron diffraction (ED) frames (Fig. 2B). The unit cell parameters were determined to be $a = b = 11.9$ Å, $c = 11.6$ Å, $\alpha = \beta = 90°$, $\gamma = 120°$, and $V = 1422.6$ Å^3. The observed reflection conditions were summarized as hkil: h-k + l = 3n; h-h0l: -h + l = 3n and hh-2hl: l = 3n, which suggest five possible space groups: R3 (no. 146), R-3 (no. 148), R32 (no. 155), R3m (no. 160), and R-3 m (no. 166). Moreover, the SAED pattern along the [0001] direction shows no mirror symmetry, indicating the Laue class of −3 and possible space groups of R3 and R-3. The single crystal structure of Pd-Te HPs was successfully solved using the space group R-3. In one unit cell, there are 60 Pd and 21 Te atoms (Fig. 2, D and E), where Pd atoms are labeled as blue spheres, while Te atoms are yellow (table S1). Viewing along the [0001] direction, atoms at (0, 0, z), (1/3, 2/3, z), and (2/3, 1/3, z) are strictly arranged into a line that is parallel to the c axis, while atoms at other positions are not. As a result, atoms are not hexagonal closed packed,
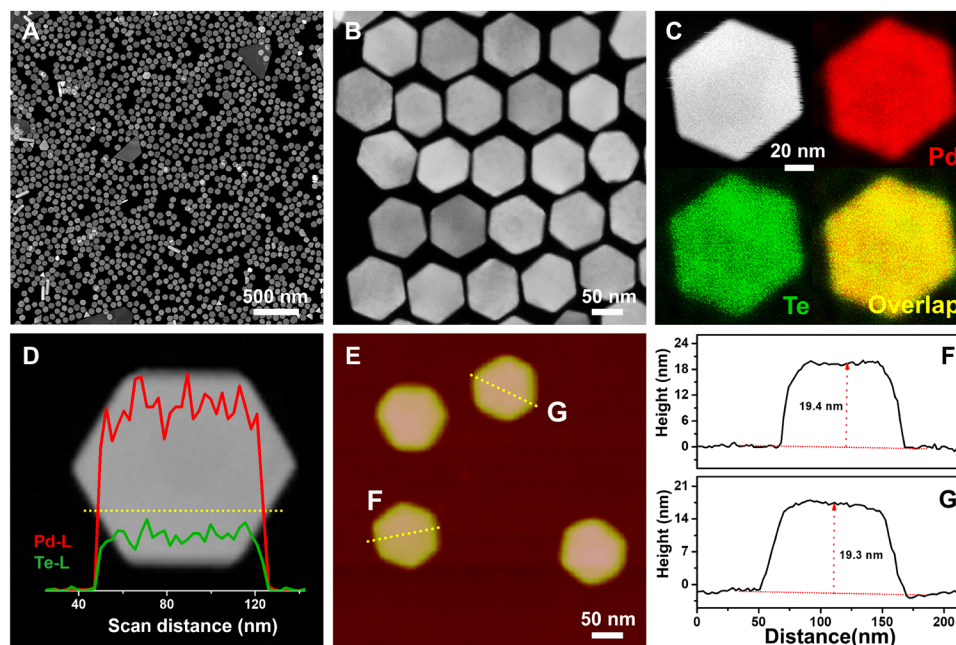
Fig. 1. Morphology characterization of Pd-Te HPs. (**A** and **B**) HAADF-STEM images and (**C**) elemental mappings of Pd-Te HPs. (**D**) Line scan of single Pd-Te HP. (**E**) AFM image and (**F** and **G**) thickness distributions of Pd-Te HPs.
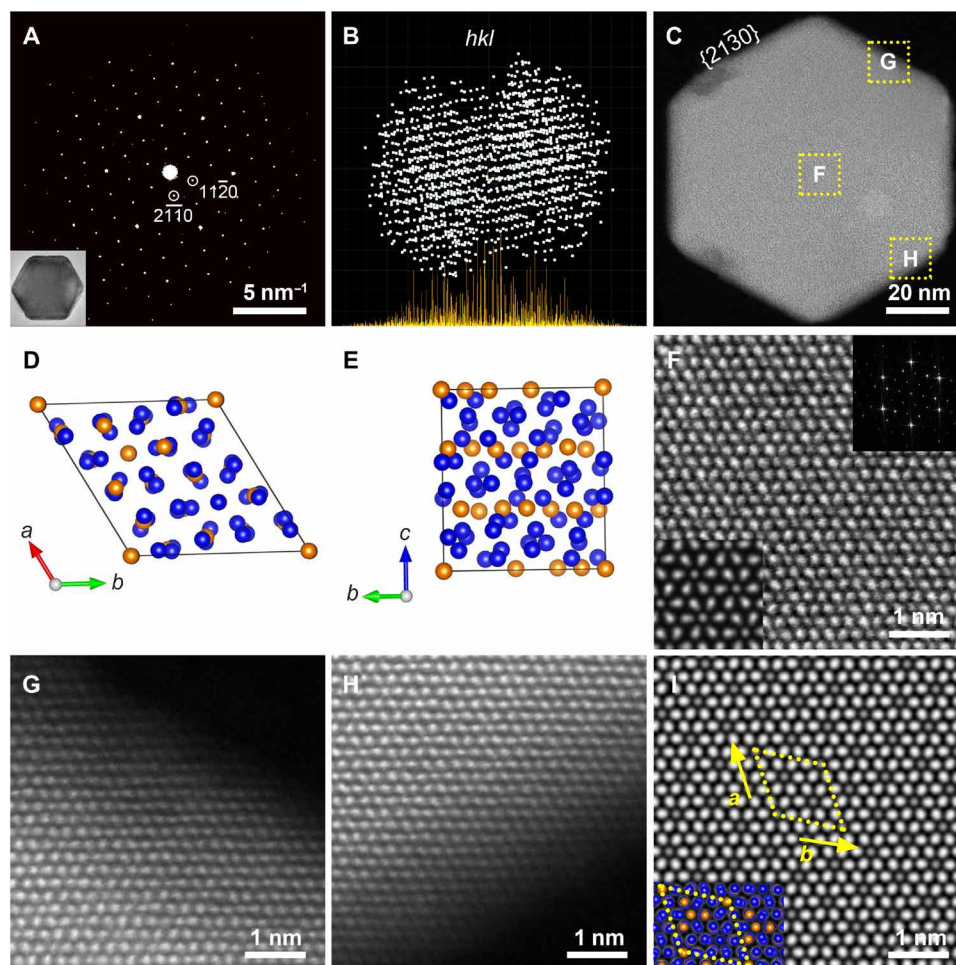
Fig. 2. Structure analysis of Pd-Te HPs. (A) SAED pattern of a single HP along the [0001] direction with TEM image. (**B**) Projection of reconstructed 3D-EDT data along a random direction. (**C**) Low-magnification HAADF-STEM image. (**D** and **E**) Solved crystal structure model viewed along the [0001] and [2$\bar{1}$$\bar{1}$0] directions. (**F** to **H**) High-resolution HAADF-STEM images taken from areas of "F," "G," and "H" in (C). Insets in (F) are simulated image with crystal thickness of 190 Å and Fourier diffractogram. (**I**) *p*6 symmetry averaged image overlaid with the structure model.

although −3 symmetry is reserved. Along the *c* axis, the crystal structure can be divided into Pd and Te layers, and Pd layers are separated by Te atomic layers. Subsequently, the structure was found to be the same as the known structure of $Pd_{20}Te_7$ (Joint Committee on Powder Diffraction Standards no.43-0810) in the Inorganic Crystal Structure Database (ICSD) (fig. S5) (*28*). To further identify the crystal structure of Pd-Te HPs, a spherical aberration corrected HAADF-STEM imaging technique was used. Figure 2C shows the HAADF image of a single Pd-Te HP along the [0001] zone axis, along with atomic-resolution images (Fig. 2, F to H) from three different areas indicated by yellow rectangles. The images show clear contrasts of different atom columns with *p*6 plane group symmetry, which matches well with the solved crystal structure, as shown in the comparison of experimental and simulated HAADF images (Fig. 2F). The *p*6 plane group symmetry averaged image (Fig. 2I) shows clearer details of the structure. The six edges of the hexagonal plate run parallel to the <4$\bar{5}$10 > directions based on the determined crystallographic axes and show a zigzag arrangement of atoms (fig. S6). The thorough structural analysis confirms the single-crystal nature of HPs with the $Pd_{20}Te_7$ phase. In particular, the positions of the Pd atoms deviate

from the ideal lattice of a hexagonal close-packed arrangement, which provides bridge sites for active catalysis centers but no effective hollow sites. This unique structure has proven be a potential candidate for excellent ORR catalytic performance and antipoisoning methanol capability.

The electrochemical properties of Pd-Te HPs were then studied and benchmarked against commercial Pt/C from Johnson Matthey [Pt/C, 20 weight % (wt %) Pt; fig. S7A] and commercial Pd/C from Sigma-Aldrich (Pd/C, 10 wt % Pd; fig. S7B). Before the electrochemical measurements, the Pd-Te HPs were loaded on commercial carbon black (C, Vulcan XC-72R) through the sonication of Pd-Te HPs and C solution (fig. S8). As the typical cyclic voltammogram (CV) curves show (Fig. 3A), the Pd-Te HPs/C shows a pair of redox peaks at high potentials that can be assigned to the redox of Te (green-shaded fill section), suggesting that the surface of Pd-Te HPs/C contains a Te element. The ORR polarization curves of different catalysts at room temperature are shown in Fig. 3B. As calculated, the half-wave potential of the Pd-Te HPs/C was 0.90 V versus reversible hydrogen electrode (RHE), which is considerably higher than those of commercial Pt/C (0.87 V) and Pd/C (0.84 V),
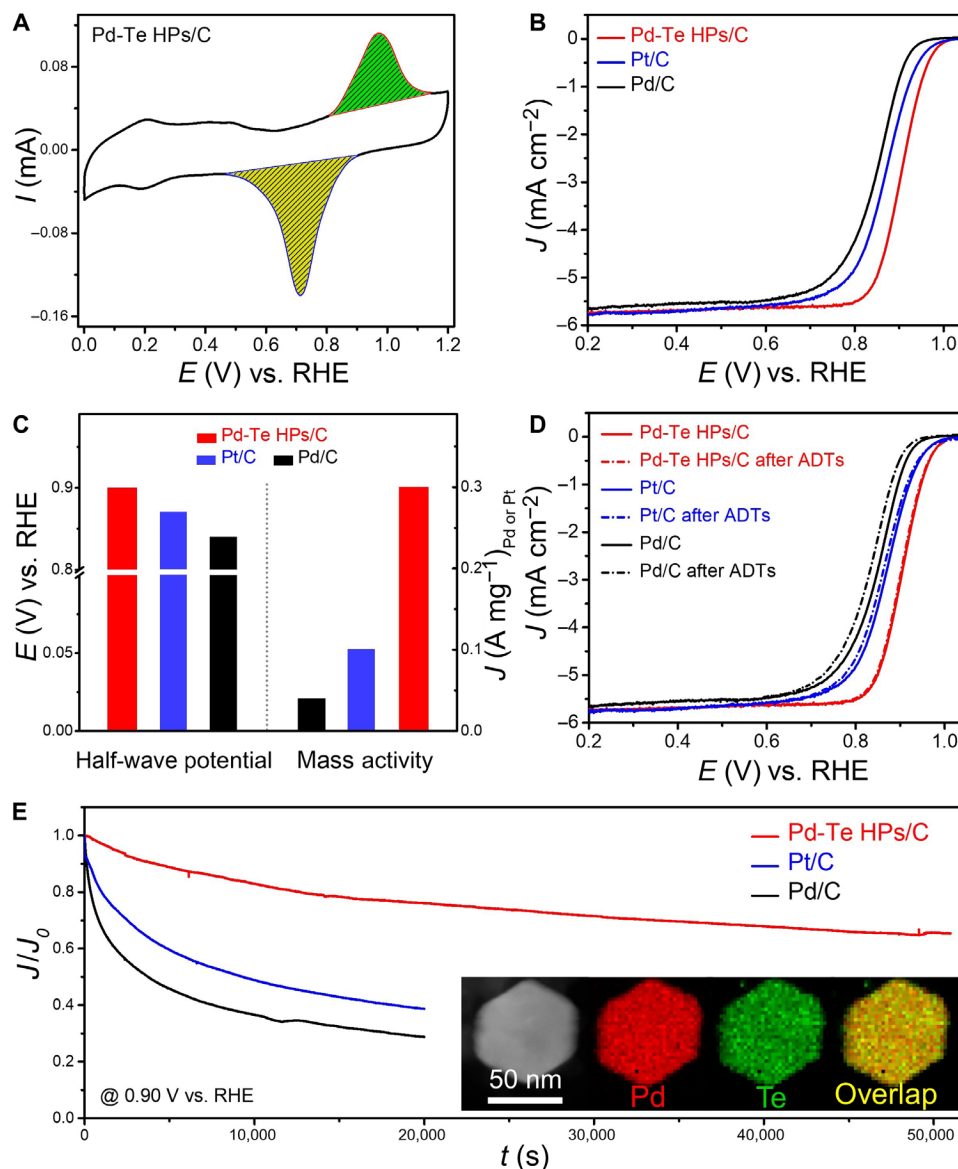
Fig. 3. Electrocatalytic performance of Pd-Te HPs/C, commercial Pt/C, and commercial Pd/C for ORR. (**A**) CV curve of Pd-Te HPs/C in 0.1 M KOH solution with a scan rate of 20 mV s^{-1}. (**B**) ORR polarization curves in O$_2$-saturated 0.1 M KOH with a scan rate of 10 mV s^{-1} and rotation speed of 1600 rpm, (**C**) histogram comparison of half-wave potential and mass activity, and (**D**) ORR polarization curves before and after 20,000 potential cycles of Pd-Te HPs/C, commercial Pt/C, and commercial Pd/C. (**E**) Chronopotentiometric responses of Pd-Te HPs/C, commercial Pt/C, and commercial Pd/C at 0.90 V versus RHE in O$_2$-saturated 0.1 M KOH. The inset in (E) is elemental mapping of Pd-Te HPs/C after chronopotentiometry for 50,000 s.

suggesting relatively high ORR activity of the Pd-Te HPs/C (Fig. 3C). Meanwhile, Pd-Te HPs/C also exhibits relatively high mass activity (0.30 A mg^{-1}) among these catalysts at 0.90 V versus RHE, which is 3.0-fold and 7.5-fold higher than commercial Pt/C (0.10 A mg^{-1}) and commercial Pd/C (0.04 A mg^{-1}), respectively. Considering the large size of Pd-Te HPs, their high mass activity is very impressive and can be further improved if their sizes can be reduced. Encouraged by the above results, we further evaluated the durability of Pd-Te HPs/C, commercial Pt/C, and commercial Pd/C by scanning 20,000 cycles in an alkaline electrolyte with sweeping potential from 0.6 to 1.0 V versus RHE. As shown in Fig. 3D, the Pd-Te HPs/C exhibits excellent durability with less than 16.0% mass activity

lost after 20,000 accelerated durability tests (ADTs). In stark contrast, the commercial Pt/C and commercial Pd/C suffered from 43.5 and 65.0% loss of mass activity after 20,000 ADTs, respectively. After 20,000 ADTs, all different electrocatalysts were also investigated by TEM, SEM-EDS, and EDS mappings, where the morphology and composition of Pd-Te HPs/C are largely maintained (fig. S9), while obvious aggregations are observed for commercial Pt/C and commercial Pd/C (fig. S10). Meanwhile, the Pd-Te HPs/C after ORR stability was analyzed by 3D-EDT (fig. S11), where the cell parameters and symmetry of the Pd-Te HPs/C after ORR stability are almost similar to that before ORR, showing the high structure stability of the Pd-Te HPs/C in the ORR condition. Furthermore, Pd-Te HPs/C

displayed outstanding stability with approximately 65% of its initial activity retained under prolonged chronopotentiometry at 0.90 V versus RHE over 50,000 s. Nevertheless, commercial Pt/C and Pd/C showed sharp activity decay, with more than 60 and 70% of their initial activity lost in only 20,000 s, respectively (Fig. 3E).

The electrocatalytic selectivity of the cathodic reaction to fuel oxidation is a very important parameter for an effective ORR electrocatalyst for fuel cell applications. In many cases, small-molecule organic fuels (i.e., CH_3OH) may cross from the anode to the cathode through the polymer electrolyte membrane, which may seriously impair the performance of the entire battery. To this end, the antipoisoning ability of Pd-Te HPs in the presence of small molecules was further investigated in ORR conditions. Initially, the CO-stripping measurements were performed as probe reactions for the study of the CO adsorption capacity for these electrocatalysts in 0.1 M KOH solution (fig. S12). It is clear that the CO adsorption peak intensity of Pd-Te HPs/C is much weaker compared with that of commercial Pt/C and Pd/C. On the other hand, the CO oxidation peak potential of Pd-Te HPs/C (0.81 V versus RHE) shifts negatively ca. 30 mV compared with commercial Pd/C (0.84 V versus RHE), illustrating that Pd-Te HPs can decrease the adsorption strength of CO compared with the counterpart of bare Pd catalyst, which facilitates the enhancement of antipoisoning capability of catalysts. The antipoisoning properties of these electrocatalysts were then evaluated by introducing CH_3OH in ORR conditions. Notably, Pd-Te HPs/C shows high tolerance to CH_3OH in an O_2-saturated solution because of low activity for MOR, while commercial Pt/C and commercial Pd/C exhibit high activity for MOR with low tolerance to CH_3OH in ORR conditions (Fig. 4, A and B, and figs. S13 and S14). Motivated by the excellent antipoisoning properties of Pd-Te HPs/C, stability tests of these catalysts were further performed

by chronoamperometric measurement after introducing CH_3OH to O_2-saturated 0.1 M KOH at 200 s. We found the current response values of Pd-Te HPs/C to be relatively stable, while the initial current response was reduced by 50% for commercial Pt/C and commercial Pd/C, confirming that Pd-Te HPs/C can maintain excellent stability even in poisoning circumstances (Fig. 4C and fig. S15). To further evaluate the ORR activity and antimethanol poisoning property of Pd-Te HPs/C, alkaline DMFC with Pd-Te HPs/C as cathode catalyst was constructed, and commercial Pt/C cathode was also tested for comparison. Figure 4 (D and E) shows the DMFC polarization curves with Pd-Te HPs/C and Pt/C as cathode catalyst, respectively. With the increasing methanol concentration ranging from 1 to 12 M, the polarization performance of Pd-Te HPs/C cathode increased when methanol concentration increased from 1 to 8 M and then declined slightly at 12 M methanol, which implies excellent methanol resistance of Pd-Te HPs/C. By contrast, commercial Pt/C cathode cannot tolerate high-concentrated methanol solution with notable performance loss when methanol concentration surpasses 2 M. Apart from improved methanol resistance, Pd-Te HPs/C also exhibited higher ORR activity. Figure 4F shows the variation of the open-circuit voltage (OCV) and maximum power density with increasing methanol concentration. At a fixed methanol concentration, such as 1 M where methanol crossover is not a limited factor for the overall DMFC performance, the OCV and peak power density of Pd-Te HPs/C cathode were notably higher than those of commercial Pt/C cathode (0.825 versus 0.718 V and 80 versus 43.9 mW cm^{-2}). Higher OCV and peak power density at all-range methanol concentration indicate that Pd-Te HPs/C has higher ORR activity than commercial Pt/C. Contributing to these two intrinsic reasons, the Pd-Te HPs/C cathode achieved the peak power density of 109 mW cm^{-2} at high methanol concentration (8 M),
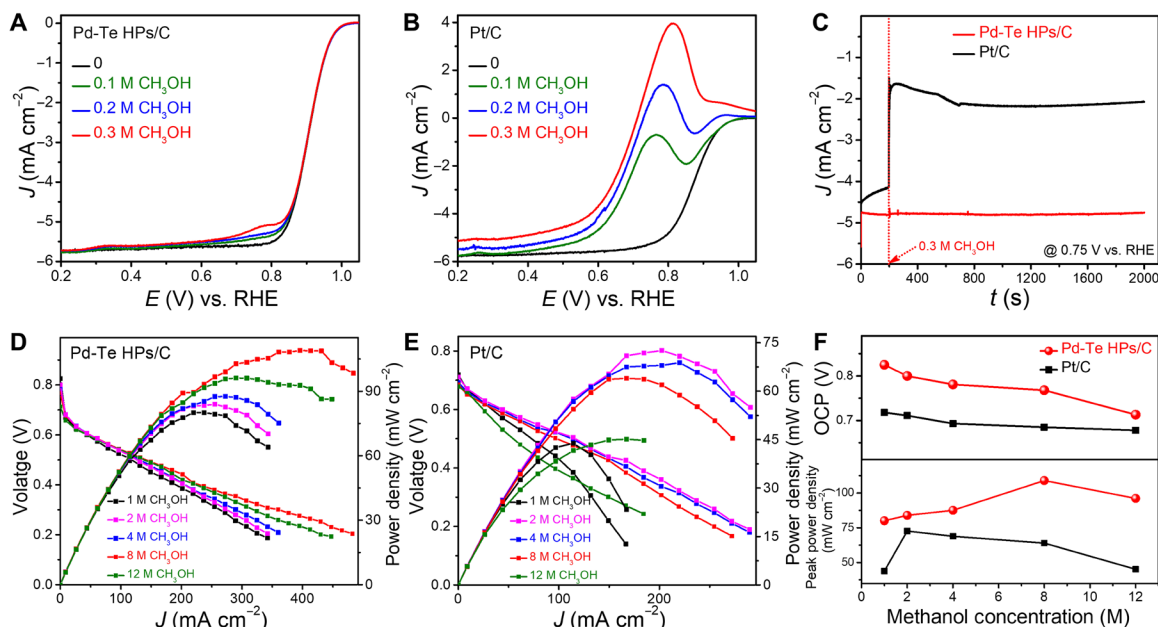
Fig. 4. Electrocatalytic performance of Pd-Te HPs/C and commercial Pt/C for methanol-tolerant ORR and DMFC. The response of (**A**) Pd-Te HPs/C and (**B**) commercial Pt/C at different CH_3OH concentrations in O_2-saturated 0.1 M KOH. (**C**) Chronoamperometric responses of Pd-Te HPs/C and commercial Pt/C by adding 0.3 M CH_3OH (at ~200 s) at 0.75 V versus RHE in O_2-saturated 0.1 M KOH. Polarization and power density curves of alkaline DMFC with (**D**) Pd-Te HPs/C and (**E**) commercial Pt/C as cathode. (**F**) Curves of OCV (up) and peak power density (down) varying with CH_3OH concentration with Pd-Te HPs/C and commercial Pt/C as cathode.

which is 1.5 times that of commercial Pt/C cathode at low methanol (2 M) concentration (72.6 mW cm^{-2}). The results strongly illustrate that Pd-Te HPs/C has excellent antimethanol poisoning performance, which is far superior to commercial Pt/C. It also implies that Pd-Te HPs/C has potential practical application in DMFC.

To understand the high ORR activity and excellent methanol-tolerant capability of the Pd-Te HPs/C, XPS and DRIFTS studies were conducted (figs. S16 and S17). The Pd 3d spectra show two peaks that can be assigned to the Pd $3d_{5/2}$ and Pd $3d_{3/2}$ states, which can be split into two doublets, associated with Pd^0 and Pd^{2+}, respectively (fig. S16A). For Te 3d spectra, the Te $3d_{5/2}$ and Te $3d_{3/2}$ can be split into two doublets, corresponding to Te^0 and Te^{4+}, respectively (fig. S16B). In addition, the dominant lines at low binding energy (Pd 3d) shift to lower binding energies, where the offset of the Pd^0 $3d_{5/2}$ peak position in Pd-Te HPs/C is ~0.28 eV compared with commercial Pd/C. The change of the electronic structure is likely associated with strong electronic interactions between Pd and Te. Simultaneously, a higher content of Pd^0 (~ 92%) in Pd-Te HPs/C was revealed, which can create more free Pd sites to enhance catalytic performance. DRIFTS spectra after exposure of Pt/C, Pd/C, and Pd-Te HPs/C to CH_3OH are shown in fig. S17. For commercial Pt/C and commercial Pd/C, besides the chemisorption bands of CH_3OH (2979, 2950, and 2920 cm^{-1}), the bands of *CO_2 (2358 cm^{-1}), *CHO (1768 and 1745 cm^{-1}), and *C-O (1200 and 1164 cm^{-1}) were also observed, which are the intermediate species of CH_3OH

decomposition (29). However, the intermediate species on Pd-Te HPs/C were not observed, with only chemisorption bands of CH_3OH observed, indicating the prominent Te contribution to the Pd-Te HPs/C is the realization of inertness to the activation of CH_3OH dissociation.

We further performed spin-polarized density functional theory (DFT) computations to gain deep insight into the high ORR activity and remarkable antipoisoning methanol properties of Pd-Te HPs (Fig. 5 and table S2). As seen in Fig. 5A, the Pd-rich (0001) facet was chosen to minimize the dangling bond of Pd atoms, and Pd atoms are arranged in a windmill-like style. In this surface model, there are no hollow sites between Pd atoms, while the bridge sties between Pd atoms could serve as the active centers for catalysis. The computational hydrogen electrode model was then used to estimate the reaction potential of electrochemical ORR and MOR processes (30). Generally, the pure thermodynamics analysis based on the free energy variations of the four element steps of ORR has been compared to determine the favorable electrochemical behaviors, and the theoretical limiting potential (U_L), the maximum applied potential at which all steps are exothermic, is largely congruent with half-wave potential in the polarization curve (31–33).

Figure 5B displays the calculated free energy diagrams along the ORR on the Pd-Te (0001) surface and the geometric structure of the key intermediates (fig. S18). It was found that the OOH* intermediate is stabilized on the top site of two Pd atoms, while OH* and O*
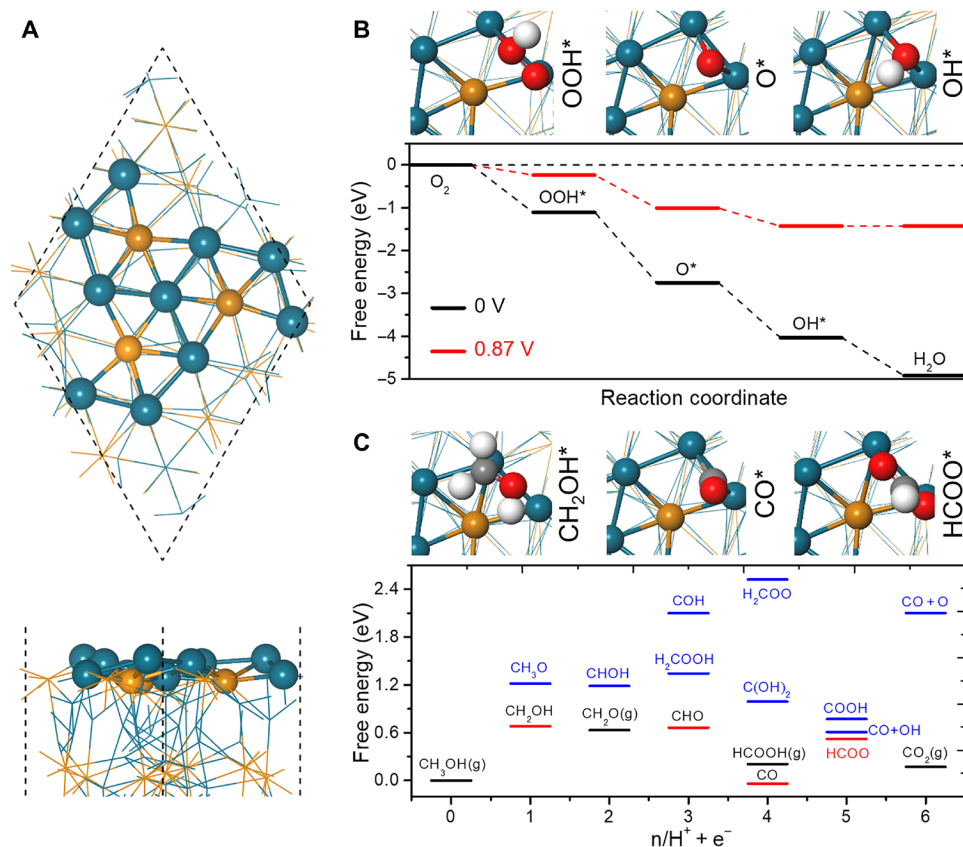

Fig. 5. Spin-polarized DFT computations of Pd-Te HPs/C. (**A**) Geometric structure in main view and side view for $Pd_{20}Te_7$ (0001) facet. Pd is shown in blue, and Te is shown in yellow. (**B**) Calculated free energy profiles at 0 and 0.87 V for ORR on $Pd_{20}Te_7$ (0001) facet, respectively. (**C**) Free energies for the possible intermediates on $Pd_{20}Te_7$ HPs during MOR. The most stable intermediates for each step are shown in red. In black are energy levels for free gas molecules. Other intermediates with high energy levels are shown in blue. The optimized structures of the key intermediates are shown above the ORR and MOR free energy diagrams, correspondingly.

intermediates are stabilized on the bridge site between two Pd atoms. According to the computations, the rate-determining step (RDS) for the ORR on Pd-Te (0001) is the conversion of OH* to a released H_2O, with a ΔG of -0.87 eV. Moreover, to give an intuitive demonstration of the superior ORR performance of Pd-Te HPs/C, we simulated its polarization curve and compared with that of Pt by means of microkinetic simulations. Both the predicted onset potential (at $J = 50$ μA cm^{-2}) and the half-wave potential outperform Pt (111) by ~0.2 V, which is consistent with experimentally observed activity trend (fig. S19). Therefore, Pd-Te HPs/C should display excellent ORR performance because it has a rather high limiting potential of 0.87 V, which is considerably higher than that of the Pt electrode (0.79 V) and actually exceeds the upper limit of the $4e^-$ ORR activity volcano (0.86 V) (34, 35). The computations also reveal that the adsorption free energy difference ($\Delta G_{OOH}* - \Delta G_{OH}*$), the value that dictates the theoretically maximum limiting potential $(4.92 - x)/2$ V, is equal to 2.93 eV, which is much lower than that of 3.2 eV for most close-packed transition metal surfaces (35). Therefore, the high ORR activity of Pd-Te HPs/C should be intrinsically attributed to $Pd_{20}Te_7$ nanostructure that breaks away from the linear relation between OOH* and OH* adsorption, which leaves sufficient room to improve catalytic activity.

The MOR activity of Pd-Te HPs was then evaluated (36, 37). Several possible pathways were considered, and the free energy profiles of the possible intermediates are shown in Fig. 5C and fig. S20. Generally, the MOR initiates the removal of an H atom from CH_3OH to form a CH_2OH* or CH_3O* intermediate. According to our computations, the formation of CH_2OH* is more energetically favorable, with a ΔG of $+0.73$ eV. Starting from CH_2OH*, the final product could be CH_2O, CO, or CO_2 following the $2e^-$, $4e^-$, and $6e^-$ oxidation pathways, respectively. Especially, for all possible pathways, the RDS is the conversion of CH_3OH to CH_2OH*. Therefore, the MOR on Pd-Te requires an external potential U of -0.73 V to ensure that all elemental steps are endothermic. For comparison, Pt only requires the external potential U of -0.37 V to trigger the oxidation of CH_3OH to CO_2 (36). Therefore, Pd-Te has a much poorer MOR activity than Pt. Actually, under the working potential of ORR ($U = 0.86$ V), all MOR elementary steps on Pd-Te would be notably suppressed, rationalizing the experimentally observed superb antimethanol poisoning property of Pd-Te HPs/C.

To summarize, well-defined Pd-Te HPs with a $Pd_{20}Te_7$ phase have been successfully fabricated to overcome the dilemma between activity and antipoisoning in DMFC, composed by a deviated hexagonal close-packed arrangement of Pd atoms in the Pd-Te nanoplates that provides bridge sites for active catalysis centers. Consequently, Pd-Te HPs/C shows promising ORR activity and high stability under prolonged chronopotentiometry for more than 50,000 s with negligible activity decay and limited structure/composition changes. Pd-Te HPs/C exhibits excellent methanol tolerance and antipoisoning stability in DMFC device, largely outperforming those of commercial Pt/C. DFT calculations verify the intrinsic contribution of the excellent performance comes from the unique surface arrangements that lead to the optimized adsorption of key intermediates within ORR as well as the high barrier of nonfavorable MOR trend. The simultaneous achievements of high activity and excellent methanol tolerance of Pd-Te HPs guarantee them as the potential electrocatalysts for DMFC and beyond. This work presents a new strategy for fabricating and designing for the 2D Pd-related catalysts with both excellent electrocatalytic activity and stability for long-term practical applications.

MATERIALS AND METHODS
Chemicals
Bis(acetylacetonate)palladium (II) [Pd(acac)$_2$, 99%], telluric (VI) acid (H$_6$TeO$_6$, 98%), and CA (99.5%) were purchased from Sigma-Aldrich. PVP (molecular weight = 58,000) was purchased from J&K. DMAC (analytical reagent) and NH$_4$Cl (analytical reagent) were purchased from Sinopharm Chemical Reagent Co. Ltd. (Shanghai, China). All the chemicals were used as received without further purification. The water (18 megohms/cm) used in all experiments was prepared by passing through an ultrapure purification system (Aqua Solutions).

Synthesis of Pd-Te HPs
In a typical preparation of Pd-Te HPs, Pd(acac)$_2$ (6.7 mg), H$_6$TeO$_6$ (2.0 mg), PVP (300.0 mg), NH$_4$Cl (8.0 mg), CA (30.0 mg), and DMAC (10 ml) were added into a reaction flask (volume, 30 ml). After ultrasonicating for around 30 min. The resulting homogeneous mixture was heated at 180°C for 2 hours in an oil bath pan before it was cooled to room temperature. The resulting products were collected by centrifugation and washed with an ethanol/acetone mixture.

Characterization
The samples were prepared by dropping ethanol dispersion of samples on carbon-coated copper transmission electron microscopy (TEM) grids using pipettes and dried under ambient condition. Low-magnification TEM was conducted on a Hitachi HT7700 transmission electron microscope at an acceleration voltage of 120 kV. High-resolution TEM, STEM, and HAADF-STEM-EDS were conducted on a JEOL GrandARM300F scanning transmission electron microscope with double Cs correctors at an acceleration voltage of 300 kV. PXRD pattern was collected on an X'Pert-Pro mean population doubling diffractometer (Netherlands PANalytical) with a Cu Kα x-ray source (λ = 1.542 Å). Low-resolution EDS was performed on a scanning electron microscope (Hitachi, S-4700). The concentration of the catalyst was determined by the inductively coupled plasma optical emission spectrometer (ICP-AES; Varian 710-ES). XPS was carried out with an Surface Science Instruments S-Probe XPS Spectrometer. The carbon peak at 284.6 eV was used as a reference to correct charging effect. The catalysts after the stability tests were collected and scratched off the electrode with the aid of sonication in ethanol for further characterization. AFM images were collected on a Bruker Dimension Icon. DRIFTS experiments were conducted at 50°C by a Nicolet 6700 Fourier transform infrared equipped with the liquid nitrogen–cooled mercury-cadmium-telluride detector. The wave number resolution is 4 cm^{-1}. The DRIFTS cell (Harrick, HVC-DRP) fitted with ZnSe windows was used as the reaction chamber. After flowing Ar (50 ml min^{-1}) for 0.5 hour, the background spectrum of the sample was acquired. CH$_3$OH/Ar (100 μl h^{-1}/50 ml min^{-1}) was then allowed to flow into the cell in turn at 50°C for 0.5 hour. The spectra were recorded after the exposure of catalysts to CH$_3$OH.

Three-dimensional electron diffraction tomography
The 3D-EDT data were collected on a 200-kV JEOL JEM2100plus TEM under the control of EDT-collect program. A high-angle tilt holder was used for the data collection. In total, 688 ED frames were recorded with the tilting angle from −60.5° to 58.7° for a typical Pd-Te HPs crystal. The data were recorded under spot size 1 with the tilt step of 0.20° and the exposure time of 0.5 s for each frame. The data were further processed by EDT-process program. The structures

of Pd-Te were solved using software SIR2014[1]. HAADF images were simulated using quantitative scanning transmission electron microscopy (QSTEM) with multislice method.

Electrochemical measurements

Before the electrochemical tests, the Pd-Te HPs dispersed in 5 ml of ethanol and Vulcan XC-72 carbon dispersed in 10 ml of ethanol were mixed and sonicated for 1 hour to make Pd-Te HPs/C. The products were collected by centrifugation and dried at 50°C. The final catalysts were redispersed in the mixture containing isopropanol and Nafion (5%) (v:v = 1:0.005) to form the homogeneous catalyst ink by sonicating for 30 min. The concentration of Pd was controlled to be 1.0 mg_{Pd}/ml based on ICP-AES measurement. Dispersion (5 μl) was transferred onto the glassy carbon (GC) electrode with the loading amount of Pd at 5 μg. The ORR measurements were performed by using a GC rotating disk electrode (RDE; Pine Research Instrumentation; diameter, 5 mm; area, 0.196 cm^2) connected to installation of rotating electrode speed control (Pine Research Instrumentation, model: AFMSRCE). A leak-free saturated calomel electrode was used as the reference electrode, and a graphite rod was used as the counter electrode. The electrolyte was 0.1 M KOH solution. The potential scan rate was 100 mV/s for the CV measurements in 0.1 M KOH solution. ORR measurements were conducted in 0.1 M KOH solutions purged with saturated O_2 during the measurements. The scan rate and rotation rate for ORR measurements were 10 mV/s and 1600 rpm, respectively. In the ORR polarization curves, the current densities were normalized in reference to the geometric area of the GC RDE (0.196 cm^2). For each catalyst, the kinetic current was normalized to only Pd (or Pt) loading to generate mass activities at 0.90 V versus RHE. The ADTs were performed at room temperature in 0.1 M KOH solution by applying the cyclic potential sweeps between 0.4 and 1.0 V versus RHE at a sweep rate of 100 mV/s for 20,000 cycles. The long-term durability tests were performed at room temperature in O_2-saturated 0.1 M KOH solution through chronoamperometric measurements for 50,000 s. The methanol tolerance tests were conducted at the same condition with ORR measurements but adding 0.1, 0.2, and 0.3 M CH_3OH into the electrolyte, respectively. The antipoisoning durability tests were performed at room temperature in O_2-saturated 0.1 M KOH and 0.3 M CH_3OH solutions through chronoamperometric measurements for 2000 s. Methanol electrooxidation measurements were conducted in 0.1 M KOH solution containing 0.3 M CH_3OH. The scan rate for methanol electrooxidation was 50 mV/s. All electrochemical experiments were performed at room temperature. For comparison, the commercial Pt/C and commercial Pd/C were used as the baseline catalysts, and the same procedures described above were applied to the electrochemical measurements.

Fabrication of membrane electrode assembly

To prepare anode catalyst ink, 4 mg of Pt-Ru/C (40 wt % Pt and 20 wt % Ru, Johnson Matthey) was added into the mixture of 100 μl of PTFE (polytetrafluoroethylene) solution (15 wt %) and 100 μl of isopropanol. After dispersing ultrasonically for 10 min, the slurry was coated on a nickel foam (1.14 cm^2) and then stored in 6 M KOH solution. The total metal (Pt + Ru) loading was 3.5 mg cm^{-2}. Similarly, 2 mg of commercial Pt/C (60 wt %) or Pd-Te HPs/C and 12 μl of Nafion solution (5 wt %) were dispersed in 600 μl of isopropanol and then coated on a gas diffusion layer to obtain cathode. To exchange H^+ in Nafion, the as-prepared cathode was immersed in

6 M KOH solution overnight. The cathode loading was 1.75 mg cm^{-2} for both catalysts. To obtain KOH-doped polybenzimidazole (PBI) membrane, the PBI membrane (20 μm) was treated by 6 M KOH solution at 80°C for 5 hours and then stored in 6 M KOH solution. Finally, the MEA was fabricated by hot pressing a Pt-Ru/C anode, a Pt/C or Pd-Te HPs/C cathode, and a KOH-doped PBI membrane at 130°C and 1 MPa for 30 s. The active area of membrane electrode assembly (MEA) was 1.14 cm^2.

Fuel cell performance test

Polarization curves were measured on a Fuel Cell Test System (850e, Scribner Associates Inc.). Anodic fuel of 6.0 M KOH + different concentrations of methanol and cathodic fuel of oxygen with 100% relative humidity were supplied at 1 ml/min and 200 sccm, respectively. The cell temperature was controlled at 80°C. After keeping the MEA under these conditions for about half an hour, a constant OCV was obtained and then followed by the polarization performance test. The polarization data were recorded in a galvanostatic polarization mode, and each point was retained for 1 min to get the steady state data.

DFT calculations

Geometric optimizations using periodic DFT were performed in the VASP code within the plane wave method and generalized gradient approximation Perdew-Burke-Ernzerhof (GGA-PBE) functional (38–42). Ultrasoft pseudopotentials were implemented to describe core electrons. Calculations were converged until energy and force components were less than 3×10^{-5} eV and 0.05 eV/Å, respectively. A 420-eV plane wave cutoff was applied for all calculations. The Γ centered K points sampling in reciprocal space with $4 \times 4 \times 1$ mesh were used. The vacuum space was set as 15 Å in z coordinate to avoid the image interaction between periodic slabs. In addition, dipole corrections and solvation effect were also included in all calculations. The calculated unit cell parameters of Pd-Te HPs (60 Pd and 21 Te atoms), $a = b = 11.9$ Å, $c = 11.6$ Å, are consistent with the experimental characterization. The Pd-terminal (0001) facet with the minimal dangling bond was chosen to be the surface model, as it closely relates to experiment. All the slabs were constructed with three layers of Pd-Te-Pd composites, of which only the top one layer was allowed to relax. The end of the two Pd sites in the windmill-like structure of the optimized (0001) facet shows the most favorable oxygen adsorption. Moreover, the d-band center obtained from the calculated PDOS (projected density of states) of the Pd-Te surface equals to −2.06 eV, which is highly consistent with the experimental measurement.

The adsorption free energy of intermediates (ΔG_{ads}) in ORR and MOR are calculated by the equation

$$\Delta G_{ads} = \Delta E_{ads} + \Delta ZPE - T\Delta S$$

where ΔE_{ads} is the adsorption energy of adsorbates, T is the ambient temperature (298.15 K), and ΔZPE and ΔS represent the zero-point energy and entropy variation, respectively. Note that the free energy correction for adsorbed species in MOR is taken from previous work, as it is accurate to treat the zero-point energies and entropies on all metals similar to Pt and the tested calculation for CH_2OH^* and CO + OH^* is in line with this assumption. Because the PBE exchange-correlation functional fails to describe the ground-state energy of O_2, CO, and CO_2 molecules, the referenced experimental data are used here. In addition, because close shell molecules

(CH_3OH, CH_2O, $HCOOH$, and CO_2) bind weakly to the surface, we use gas-phase value to represent the free energy of these intermediates (*43*).

SUPPLEMENTARY MATERIALS

Supplementary material for this article is available at http://advances.sciencemag.org/cgi/content/full/6/31/eaba9731/DC1

REFERENCES AND NOTES

1. B. C. Steele, A. Heinzel, Materials for fuel-cell technologies. *Nature* **414**, 345–352 (2001).
2. M. K. Debe, Electrocatalyst approaches and challenges for automotive fuel cells. *Nature* **486**, 43–51 (2012).
3. J. R. Varcoe, R. C. T. Slade, Prospects for alkaline anion-exchange membranes in low temperature fuel cells. *Fuel Cells* **5**, 187–200 (2005).
4. Y. Jiao, Y. Zheng, M. Jaroniec, S. Z. Qiao, Design of electrocatalysts for oxygen- and hydrogen-involving energy conversion reactions. *Chem. Soc. Rev.* **44**, 2060–2086 (2015).
5. E. Antolini, Palladium in fuelcell catalysis. *Energ. Environ. Sci.* **2**, 915–931 (2009).
6. C. Bianchini, P. K. Shen, Palladium-based electrocatalysts for alcohol oxidation in half cells and in direct alcohol fuel cells. *Chem. Rev.* **109**, 4183–4206 (2009).
7. G. He, Z. Li, J. Zhao, S. Wang, H. Wu, M. D. Guiver, Z. Jiang, Nanostructured ion-exchange membranes for fuel cells: Recent advances and perspectives. *Adv. Mater.* **27**, 5280–5295 (2015).
8. Y. Feng, H. Liu, J. Yang, A selective electrocatalyst-based direct methanol fuel cell operated at high concentrations of methanol. *Sci. Adv.* **3**, e1700580 (2017).
9. A. Rabis, P. Rodriguez, T. J. Schmidt, Electrocatalysis for polymer electrolyte fuel cells: Recent achievements and future challenges. *ACS Catal.* **2**, 864–890 (2012).
10. W. Wang, F. Lv, B. Lei, S. Wan, M. Luo, S. Guo, Tuning nanowires and nanotubes for efficient fuel-cell electrocatalysis. *Adv. Mater.* **28**, 10117–10141 (2016).
11. Y. Nie, L. Li, Z. Wei, Recent advancements in Pt and Pt-free catalysts for oxygen reduction reaction. *Chem. Soc. Rev.* **44**, 2168–2201 (2015).
12. A. Morozan, B. Jousselme, S. Palacin, Low-platinum and platinum-free catalysts for the oxygenreduction reaction at fuelcell cathodes. *Energ. Environ. Sci.* **4**, 1238–1254 (2011).
13. X. Huang, Z. Zhao, L. Cao, Y. Chen, E. Zhu, Z. Lin, M. Li, A. Yan, A. Zettl, Y. M. Wang, X. F. Duan, T. Mueller, Y. Huang, High-performance transition metal–doped Pt₃Ni octahedra for oxygen reduction reaction. *Science* **348**, 1230–1234 (2015).
14. Y. Kang, X. Ye, J. Chen, Y. Cai, R. E. Diaz, R. R. Adzic, E. A. Stach, C. B. Murray, Design of Pt–Pd binary superlattices exploiting shape effects and synergistic effects for oxygen reduction reactions. *J. Am. Chem. Soc.* **135**, 42–45 (2013).
15. M.-H. Shao, K. Sasaki, R. R. Adzic, Pd–Fe nanoparticles as electrocatalysts for oxygen reduction. *J. Am. Chem. Soc.* **128**, 3526–3527 (2006).
16. L. Xiao, L. Zhuang, Y. Liu, J. Lu, H. D. Abruña, Activating Pd by morphology tailoring for oxygen reduction. *J. Am. Chem. Soc.* **131**, 602–608 (2008).
17. W. Huang, X.-Y. Ma, H. Wang, R. Feng, J. P. Zhou, N. Duchesne, P. Zhang, F. Chen, N. Han, F. Zhao, J. Zhou, W.-B. Cai, Y. Li, Promoting effect of Ni(OH)₂ on palladium nanocrystals leads to greatly improved operation durability for electrocatalytic ethanol oxidation in alkaline solution. *Adv. Mater.* **29**, 1703057 (2017).
18. A. Kowal, M. Li, M. Shao, K. Sasaki, M. B. Vukmirovic, J. Zhang, N. S. Marinkovic, P. Liu, A. I. Frenkel, R. R. Adzic, Ternary Pt/Rh/SnO₂ electrocatalysts for oxidizing ethanol to CO₂. *Nat. Mater.* **8**, 325–330 (2009).
19. L. Bu, S. Guo, X. Zhang, X. Shen, D. Su, G. Lu, X. Zhu, J. Yao, J. Guo, X. Huang, Surface engineering of hierarchical platinum-cobalt nanowires for efficient electrocatalysis. *Nat. Commun.* **7**, 11850 (2016).
20. K. Bleakley, P. Hu, A density functional theory study of the interaction between CO and O on a Pt Surface: CO/Pt(111), O/Pt(111), and CO/O/Pt(111). *J. Am. Chem. Soc.* **121**, 7644–7652 (1999).
21. A. Cuesta, At least three contiguous atoms are necessary for CO formation during methanol electrooxidation on platinum. *J. Am. Chem. Soc.* **128**, 13332–13333 (2006).
22. M.-R. Gao, Y.-F. Xu, J. Jiang, S.-H. Yu, Nanostructured metal chalcogenides: Synthesis, modification, and applications in energy conversion and storage devices. *Chem. Soc. Rev.* **42**, 2986–3017 (2013).
23. L. Fu, D. Hu, R. G. Mendes, M. H. Rümmeli, Q. Dai, B. Wu, L. Fu, Y. Liu, Highly organized epitaxy of dirac semimetallic PtTe₂ crystals with extrahigh conductivity and visible surface plasmons at edges. *ACS Nano* **12**, 9405–9411 (2018).
24. H. Ma, P. Chen, B. Li, J. Li, R. Ai, Z. Zhang, G. Sun, K. Yao, Z. Lin, B. Zhao, R. Wu, X. Tang, X. Duan, X. Duan, Thickness-tunable synthesis of ultrathin type-II dirac semimetal PtTe₂ single crystals and their thickness-dependent electronic properties. *Nano Lett.* **18**, 3523–3529 (2018).
25. X. Chia, A. Adriano, P. Lazar, Z. Sofer, J. Luxa, M. Pumera, Layered platinum dichalcogenides (PtS₂, PtSe₂, and PtTe₂) electrocatalysis: Monotonic dependence on the chalcogen size. *Adv. Funct. Mater.* **26**, 4306–4318 (2016).
26. Y. Wang, Y. Li, T. Heine, PtTe monolayer: Two-dimensional electrocatalyst with high basal plane activity toward oxygen reduction reaction. *J. Am. Chem. Soc.* **140**, 12732–12735 (2018).
27. M. Gemmi, P. Oleynikov, Scanning reciprocal space for solving unknown structures: Energy filtered diffraction tomography and rotation diffraction tomography methods. *Z. Kristallogr.* **228**, 51–58 (2013).
28. W. S. Kim, G. Y. Chao, L. J. Cabri, Phase relations in the Pd-Te system. *J. Less Common Met.* **162**, 61–74 (1990).
29. J. Greeley, M. Mavrikakis, Competitive paths for methanol decomposition on Pt(111). *J. Am. Chem. Soc.* **126**, 3910–3919 (2004).
30. J. K. Nørskov, J. Rossmeisl, A. Logadottir, L. R. K. J. Lindqvist, J. R. Kitchin, T. Bligaard, H. Jónsson, Origin of the overpotential for oxygen reduction at a fuel-cell cathode. *J. Phys. Chem. B* **108**, 17886–17892 (2004).
31. S. Siahrostami, A. Verdaguer-Casadevall, M. Karamad, D. Deiana, P. Malacrida, B. Wickman, M. Escudero-Escribano, E. A. Paoli, R. Frydendal, T. W. Hansen, I. Chorkendorff, I. E. L. S. Stephens, J. Rossmeisl, Enabling direct H₂O₂ production through rational electrocatalyst design. *Nat. Mater.* **12**, 1137–1143 (2013).
32. A. Verdaguer-Casadevall, D. Deiana, M. Karamad, S. Siahrostami, P. Malacrida, T. W. Hansen, J. Rossmeisl, I. Chorkendorff, I. E. Stephens, Trends in the electrochemical synthesis of H₂O₂: Enhancing activity and selectivity by electrocatalytic site engineering. *Nano Lett.* **14**, 1603–1608 (2014).
33. G.-L. Chai, Z. Hou, D.-J. Shu, T. Ikeda, K. Terakura, Active sites and mechanisms for oxygen reduction reaction on nitrogen-doped carbon alloy catalysts: Stone–wales defect and curvature effect. *J. Am. Chem. Soc.* **136**, 13629–13640 (2014).
34. V. Tripković, E. Skúlason, S. Siahrostami, J. K. Nørskov, J. Rossmeisl, The oxygen reduction reaction mechanism on Pt(111) from density functional theory calculations. *Electrochim. Acta* **55**, 7975–7981 (2010).
35. V. Viswanathan, H. A. Hansen, J. Rossmeisl, J. K. Nørskov, Universality in oxygen reduction electrocatalysis on metal surfaces. *ACS Catal.* **2**, 1654–1660 (2012).
36. P. Ferrin, A. U. Nilekar, J. Greeley, M. Mavrikakis, J. Rossmeisl, Reactivity descriptors for direct methanol fuel cell anode catalysts. *Surf. Sci.* **602**, 3424–3431 (2008).
37. P. Ferrin, M. Mavrikakis, Structure sensitivity of methanol electrooxidation on transition metals. *J. Am. Chem. Soc.* **131**, 14381–14389 (2009).
38. M. C. Burla, R. Caliandro, B. Carrozzini, G. L. Cascarano, C. Cuocci, C. Giacovazzo, M. Mallamo, A. Mazzone, G. Polidori, Crystal structure determination and refinement via SIR2014. *J. Appl. Cryst.* **48**, 306–309 (2015).
39. G. Kresse, J. Furthmüller, Efficiency of ab-initio total energy calculations for metals and semiconductors using a plane-wave basis set. *J. Comput. Mater. Sci.* **6**, 15–50 (1996).
40. P. E. Blöchl, Projector augmented-wave method. *Phys. Rev. B* **50**, 17953–17979 (1994).
41. G. Kresse, D. Joubert, From ultrasoft pseudopotentials to the projector augmented-wave method. *Phys. Rev. B* **59**, 1758–1775 (1999).
42. J. P. Perdew, K. Burke, M. Ernzerhof, Generalized gradient approximation made simple. *Phys. Rev. Lett.* **77**, 3865–3868 (1996).
43. Y. Li, H. Su, S. H. Chan, Q. Sun, CO₂ electroreduction performance of transition metal dimers supported on graphene: A theoretical study. *ACS Catal.* **5**, 6658–6664 (2015).

Science Advances

Atomically deviated Pd-Te nanoplates boost methanol-tolerant fuel cells

Ying Zhang, Bolong Huang, Gan Luo, Tu Sun, Yonggang Feng, Yucheng Wang, Yanhang Ma, Qi Shao, Yafei Li, Zhiyou Zhou and Xiaoqing Huang

ARTICLE TOOLS	http://advances.sciencemag.org/content/6/31/eaba9731
SUPPLEMENTARY MATERIALS	http://advances.sciencemag.org/content/suppl/2020/07/27/6.31.eaba9731.DC1
REFERENCES	This article cites 43 articles, 2 of which you can access for free http://advances.sciencemag.org/content/6/31/eaba9731#BIBL
PERMISSIONS	http://www.sciencemag.org/help/reprints-and-permissions

Use of this article is subject to the Terms of Service